Electronic Supplementary Material (ESI) for Physical Chemistry Chemical Physics.
This journal is © the Owner Societies 2018

Sample preparation

Samples of $K_2[Fe(bpy)(CN)_4]$ (Schilt 1960) and $TBA_2[Fe(bpy)(CN)_4]$ (Toma 1983) were prepared according to literature procedures. $K_2[Fe(bpy)(CN)_4]$ was used for aqueous solution experiments, $TBA_2[Fe(bpy)(CN)_4]$ was used for experiments in DMSO.

High fluence TA measurements

TA measurements of 500 nm excitation in water were conducted at excitation pulse energies of 1.6 µJ and 6.4 µJ and fluences of approximately of $4x10^{11}$ W/cm^2 and $2x10^{12}$ W/cm^2, respectively. The recorded data is presented in the Figure S1A,B respectively. It is seen that the amplitude of all transient features below 550 nm increase by around a factor of four, while the long-lived positive feature at 680 nm becomes significantly more pronounced.

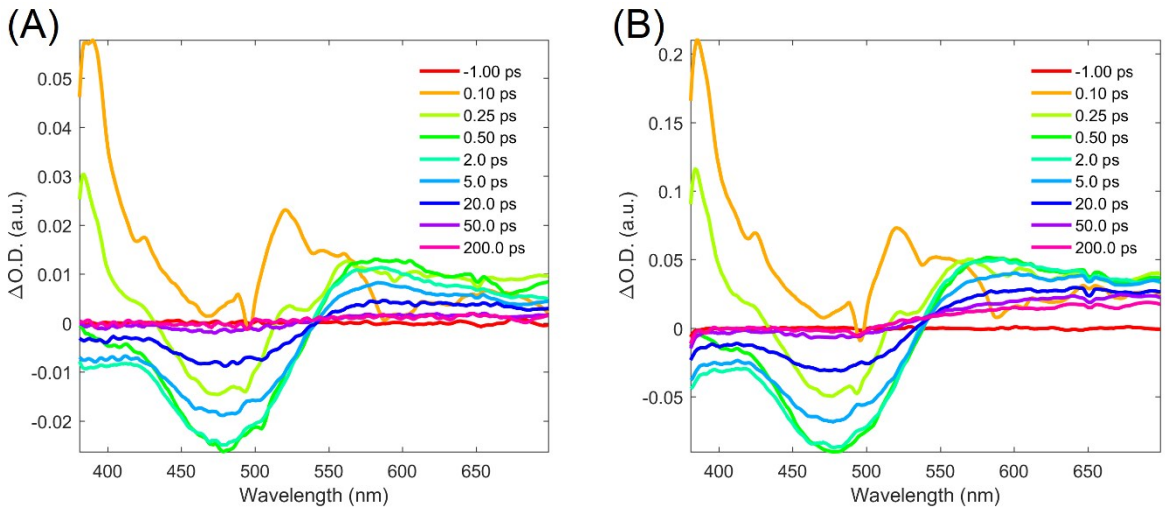

Figure S1. Transient absorption spectra of $[Fe(bpy)(CN)_4]^{2-}$ at selected time delays in H_2O excited at 500 nm with 1.6 µJ (A) and 6.4 µJ (B) pulse energy.

Global analysis of the data allows us to retrieve the amplitude and time scales of the dynamic processes observed in the data. We find that the positive feature of SAS1 and the negative feature of SAS2 both increase by a factor of 3.6, slightly below the factor of four excitation fluency increase. Meanwhile the positive feature of SAS3 increases by a factor of 15 (from a ΔO.D. of 0.0014 to 0.021), very close to the expected factor of 16 increase from a 2-photon process.

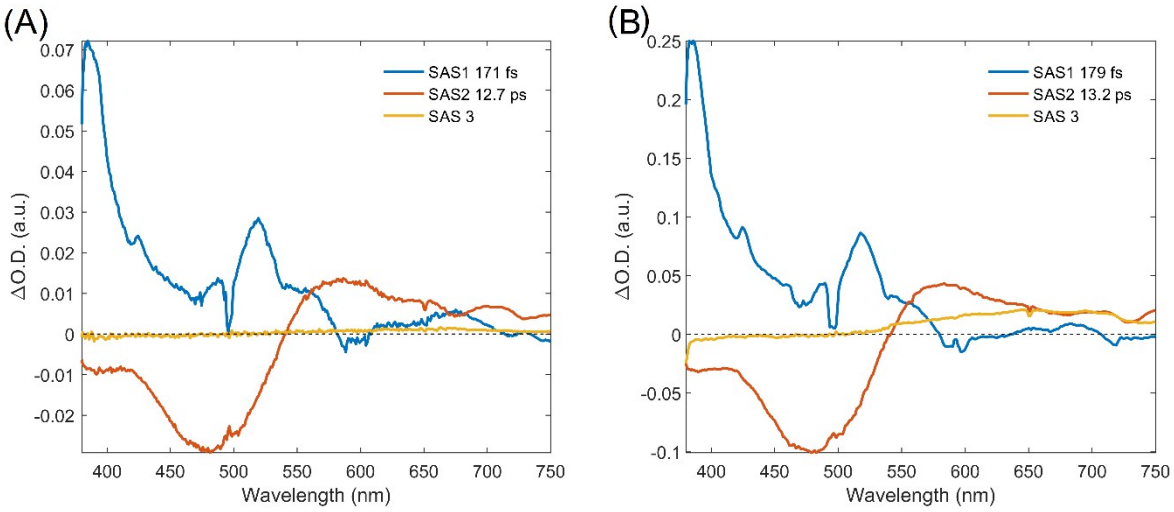

Figure S2. Species associated spectra returned from the global analysis of the $[Fe(bpy)(CN)_4]^{2-}$ transient absorption in H_2O, excited at 500 nm with 1.6 µJ (A) and 6.4 µJ (B) excitation pulse energy.

It is also seen that the shape of SAS1 and SAS2 from the two measurements are practically identical, and that the extracted time scales are well within the error of each other: $SAS1_{4mj}$ 171 ± 32 fs, $SAS2_{4mJ}$ 12.7 ± 0.4 ps $SAS1_{16mj}$ 179 ± 38 fs, $SAS2_{16mJ}$ 13.2 ± 0.3 ps

The yield of photoionization can be estimated by comparing the amplitude of the GSB and solvated electron absorption, to their molar extinction coefficients at their absorption maximum (2500 $M^{-1}cm^{-1}$ and 20000 $M^{-1}cm^{-1}$ (Lenchenkov 2001)), respectively). For the low fluence data in Figure S2A, the amplitude of these features (0.029 and 0.0014 O.D. respectively) shows that the photoionization quantum yield is 0.006 ± 0.001, well below 1%. The low quantum yield of photoionization for these low fluence measurements means that the influence of the photoionization on the excited state cascade is negligible.

Laser fluence measurements for XES experiments

For the XES measurements conducted at 400 nm excitation in water the laser flounce was scanned to ensure that experiments were conducted before the onset of higher order excitation events asides from the first order excitation and second order photoionization events observed by the TA experiments. The integrated XES difference signal intensity at 5 ps time delay as a function excitation fluence is presented in Figure S3. A linear

fit of the difference signal intensity as a function of fluence (red line) shows weak deviation above 8 μJ, and significant deviation above 15 μJ. The, transient experiments were conducted at 12.5μJ, before the onset of significant deviation from a linear relationship between excitation fluence and difference signal.

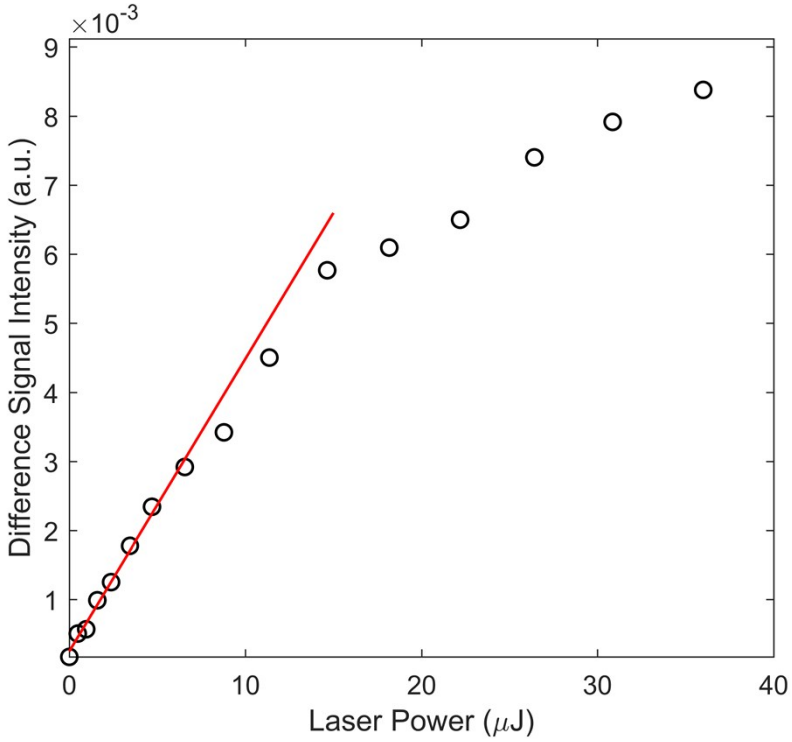

Figure S3, XES difference signal intensity at 5 ps time delay as a function excitation fluence is (black circles), and linear fit at low fluence (red line).

Identifying the slow time scale in the XES ground state recovery

Previous work that monitored signatures of the bipyridine radical anion demonstrated that solvated electrons are scavenged by ground state $[Fe(bpy)(CN)_4]^{2-}$ to form $[Fe(bpy)(CN)_4]^{3-}$, and that ground state recovery is a recombination of $[Fe(bpy)(CN)_4]^{3-}$ and $[Fe(bpy)(CN)_4]^{-}$ to from $[Fe(bpy)(CN)_4]^{2-}$ (Horváth 1991). Horváth et al. determined the rate constant of the scavenging of solvated electrons ($e^-(aq) + [Fe(bpy)(CN)_4]^{2-} \rightarrow [Fe(bpy)(CN)_4]^{3-}$) is $k = 1.3x10^{10}$ $M^{-1}s^{-1}$, while the rate constant of charge recombination ($[Fe(bpy)(CN)_4]^{-} + [Fe(bpy)(CN)_4]^{3-} \rightarrow [Fe(bpy)(CN)_4]^{2-}$) is $k = 1.8x10^{10}$ $M^{-1}s^{-1}$. (Horváth 1991) Given the concentrations used in the present study, this translates to a few nanosecond characteristic timescale for the formation of $[Fe(bpy)(CN)_4]^{3-}$ and a hundreds-of-nanosecond timescale for the secondary charge recombination. For the reduced species,

$[Fe(bpy)(CN)_4]^{3-}$, the electron resides on the bipyridine ligand, such that the iron center is a formal Fe(II) species and the XES signal is expected to be extremely similar to that of the ground state. Thus, both Kα and Kβ measurements are expected to be insensitive to the $[Fe(bpy)(CN)_4]^{3-}$, as indicated by the lack of dynamics on the few nanosecond time scale where the species is formed. Thus, the long time scale dynamics only tracks the loss of $[Fe(bpy)(CN)_4]^{-}$ upon reformation of ground state.

The time evolution of the decay kinetic describing recombination is a 2nd order reaction (involving $[Fe(bpy)(CN)_4]^{-}$ and $[Fe(bpy)(CN)_4]^{3-}$, formed in equal amounts after few nanoseconds), expressed as $[A] = \frac{1}{\frac{1}{[A]_0} + kt}$. Comparative fits to the long time delay data using first and second order rate expressions for the decay are illustrated in Figure 5 as inserts (A) and (B), respectively. Second order decay kinetics provide an overall better description of the data and captures the incomplete recovery observed within the 3 µs time window of the experiment. From the fit shown in Figure 5b we obtain a rate constant of 1.1 ± 0.8x10^{10} M^{-1}s^{-1} and an initial concentration of $[Fe(bpy)(CN)_4]^{-}$ of 1.8 ± 1 mM. The fitted rate constant matches the literature value of 1.8 ± 0.4x10^{10} M^{-1}s^{-1}, and the initial $[Fe(bpy)(CN)_4]^{-}$ concentration is in good agreement with the total excitation fraction, as we will be show in the following.

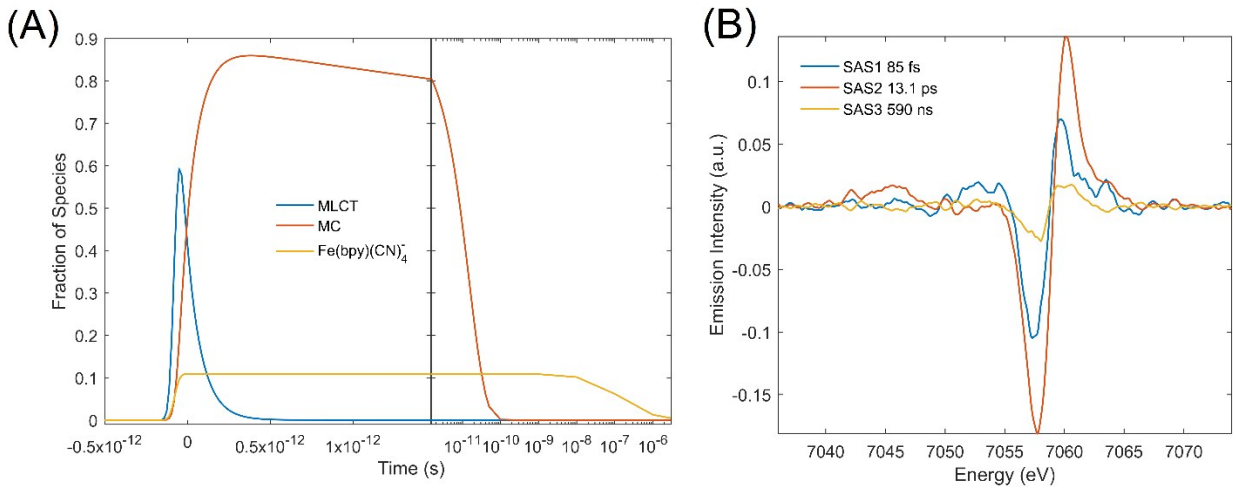

Figure S4 The time-evolution of the $[Fe(bpy)(CN)_4]^{2-}$ species in the excited state cascade as derived from the analysis of the Kα and optical TA data (A), and their respective SAS derived from global analysis of the Kβ data (B).

SAS3, associated with the long lived third species, is compared to SAS1 and SAS2 in Figure 7c. Since SAS1 and SAS3 describe a very similar species with respect to the Fe center, the scaling factor that yields the best

agreement between the two can be used to calculate the photoionization yield. The best-fit scaling factor is a multiplication of SAS3 by 6.3. This indicates that 84% of the photoinitiated cascade progresses through the MLCT and ^{3}MC state before returning to the ground state, and 16% undergoes photoionization and eventual recombination with $[Fe(bpy)(CN)_4]^{3-}$. Using this model for the excited state cascade, the excitation fraction can be retrieved as the scaling factor between the MLCT reference and the sum of SAS1 and SAS3. Alternatively, it can be retrieved as the sum of the scaling factor between the MLCT reference and SAS3 plus the scaling factor between the ^{3}MC reference and SAS2. Both estimates return an excitation faction of 33%. With an $[Fe(bpy)(CN)_4]^{2-}$ concentration of 50 mM, an excitation fraction of 33%, and a 16% photoionization fraction, the initial absolute concentration of $[Fe(bpy)(CN)_4]^{3-}$ is calculated to be 2.3 mM. This is in good agreement with the 1.8 ± 1 mM retrieved from the recombination time quantified in the Kα kinetics.

As a final note, we stress that, neither $e^-(aq)$ nor $[Fe(bpy)(CN)_4]^{3-}$ contribute to the total difference signal measured by (Kα and Kβ) XES. Therefore, only the oxidized $[Fe(bpy)(CN)_4]^-$ photoproduct is included in the analysis of the Kα and Kβ data.

Timing diagnostics

The shot-to-shot x-ray-optical relative time of arrival fluctuations were measured for every x-ray-optical pulse pair with a timing diagnostic tool based on optical detection of x-ray generated carriers in a Si3N4 thin film (Harmand). This experimental measure of the relative timing was used to sort each experimental shot by the relative time of arrival. Thus, the final time resolution of the experiment results from the convolution of the optical and x-ray pulse durations, the difference group velocity of the x-ray and optical pulses in the sample, and the error in the relative time of arrival measurement. These set the resolution to roughly 80 fs FWHM.

XES Data Treatment

The CSPAD detectors recording the Kα and Kβ fluorescence were calibrated through a pixel dependent dark current (pedestal) subtraction, a common mode off-set subtraction, and an experimentally determined gain map. The gain map was built from histograms of the response of each pixel in all datasets used in the analysis, after dark current and common mode subtraction. Gaussians were fit to the zeroth, first, second, and third photon peaks of the histograms, enabling fine-tuned dark and gain corrections directly from the data. The zero-

photon peaks were centered at zero analog-to-digital units (ADU) and the separation between photon peaks were scaled to unity for all pixels. To remove the zero-photon read-out noise, all ADU values below a threshold of 3σ of the zero-photon peak were set to zero.

At this stage in the data analysis, each pump-probe event is associated with a Kα and a Kβ detector image which reflects the number of photons seen by each pixel. For both the Kα and Kβ signal, difference images are constructed by scaling each image to the incident photon energy, and subtracting the average signal recorded for the optical laser-off x-ray exposures associated with the nominal time step from which each individual pump-probe event was recorded.

Average difference images are then constructed from all pump-probe events belonging to the same time-bin as sorted by the nominal time-delay and the timing tool correction value. The Kα difference signal of each time bin is then given by the integrated average difference image of that time bin. The Kβ difference signal of each time bin is obtained by integrating the difference image along the nondispersive axis of the detector.

Kβ XES data correction

Misalignment of one of the four analyzer crystals of the multicrystal spectrometer during the LCLS experiment resulted in distorted Kβ XES spectra. In order to remove this distortion the spectra were corrected with a following formula

$$S_{corr} = FT^{-1}\left\{\frac{FT\{D^*\}FT\{S_{uncorr}\}}{FT\{D^*\}FT\{D\}}\right\}$$

S_{corr} is the corrected spectrum, S_{uncorr} is uncorrected (measured) spectrum and D is the function describing the distortion defined by two delta peaks whose relative height and position correspond to misalignment of the fourth crystal. Note that direct application of the deconvolution theorem would result in singularities and therefor before the division is carried out both nominator and denominator are multiplied by $FT\{D^*\}$. The correction procedure includes finding the suitable relative height and shift of the two delta peaks in D.

Computational Chemistry

The ground state (S0), ^{3}MLCT, ^{3}MC, ^{5}MLCT, and ^{5}MC geometries of the complex were fully reoptimized from recently presented DFT structures (Zhang 2016) without symmetry constraints using the B3LYP* hybrid DFT functional (Reiher 2001) together with the standard triple-ζ 6-311G(d,p) basis set (Dunning 1977), and with a complete acetonitrile or water polarizable continuum model (PCM) (Tomasi 2005) in Gaussian G09. (Frish 2016) A secondary series of calculations estimating the effects of specific solvation interactions in water were conducted by also including four explicit water molecules, arranged with a hydrogen pointing towards each of the nitrogen lone-pairs of the CN^- ligands, and with the full system comprising the complex plus explicit water molecules immersed in a PCM water solvent model. The fully optimized excited state local minima of the respective state multiplicities were identified and could be clearly distinguished on the basis of the spin density on the Fe atom, and bpy ligand. The following table presents the energies of the different excited states with respect to the ground state energy for the three different solvent environments.

ESI Table 1. Calculated optimized state energies in different solvent environments.

State*	DMSO(s)	H_2O(s)	$(H_2O)_4$/H2O(s)	$\Delta E_{Sp.Solv}$**
S0	0.00	0.00	0.00	0
^{3}MLCT	1.04	1.07	1.32	+0.25
^{3}MC	1.03	1.03	1.16	+0.13
^{5}MC	1.41	1.41	1.58	+0.17

* State energies for different solvent environments are given (in eV) relative to the respective S0 energy for that solvent environment.

** Energy change arising from specific solvation interactions $\Delta E_{Sp.Solv}$ is defined as the energy difference between PCM water, and PCM water + 4 H_2O

The explicit energy change upon specific solvation ($\Delta E_{Sp.Solv}$) for the S0, ^{3}MLCT, ^{3}MC, and ^{5}MC states qualitatively reproduce the experimental assignment illustrated in Figure 7D: All states are destabilized relative to the ground state, the ^{3}MLCT is destabilized the most, and the ^{3}MC state is destabilized the least. The relaxed energy minimum structures shows that the explicit waters form hydrogen-like bonds to the cyanide nitrogen lone pairs. This is illustrated for the ground state structure in Figure S5.

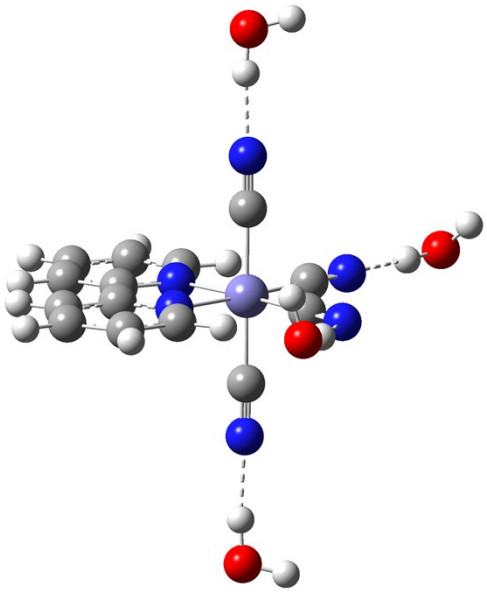

Figure S5 Relaxed ground state energy minimum structure of $[Fe(bpy)(CN)_4]^{2-}$ with 4 explicit water molecules resulting from the DFT calculations.

References

(Dunning 1977) T.H. Dunning, P.J. Hay, 1977, "Gaussian basis sets for molecular calculations," in: "Modern Theoretical Chemistry," vol. 3. Ed. H.F. Schaefer III, pp. 1-28, Plenum Press, New York.

(Frish 2016) Gaussian 09, Revision A.02, M. J. Frisch, G. W. Trucks, H. B. Schlegel, G. E. Scuseria, M. A. Robb, J. R. Cheeseman, G. Scalmani, V. Barone, G. A. Petersson, H. Nakatsuji, X. Li, M. Caricato, A. Marenich, J. Bloino, B. G. Janesko, R. Gomperts, B. Mennucci, H. P. Hratchian, J. V. Ortiz, A. F. Izmaylov, J. L. Sonnenberg, D. Williams-Young, F. Ding, F. Lipparini, F. Egidi, J. Goings, B. Peng, A. Petrone, T. Henderson, D. Ranasinghe, V. G. Zakrzewski, J. Gao, N. Rega, G. Zheng, W. Liang, M. Hada, M. Ehara, K. Toyota, R. Fukuda, J. Hasegawa, M. Ishida, T. Nakajima, Y. Honda, O. Kitao, H. Nakai, T. Vreven, K. Throssell, J. A. Montgomery, Jr., J. E. Peralta, F. Ogliaro, M. Bearpark, J. J. Heyd, E. Brothers, K. N. Kudin, V. N. Staroverov, T. Keith, R. Kobayashi, J. Normand, K. Raghavachari, A. Rendell, J. C. Burant, S. S. Iyengar, J. Tomasi, M. Cossi, J. M. Millam, M. Klene, C. Adamo, R. Cammi, J. W. Ochterski, R. L. Martin, K. Morokuma, O. Farkas, J. B. Foresman, and D. J. Fox, Gaussian, Inc., Wallingford CT, 2016.

(Horváth 1991) Horváth, A., Szõke, J. & Wojnárovits, L. Mechanism of photoinduced redox reactions in aqueous solutions of $[Fe(bpy)(CN)4]^{2-}$. *Inorganica Chim. Acta*, 1991, **179,** 97–104.

(Lenchenkov 2001) Lenchenkov et al. Chemical Physics Letters, 2001, **342**, 277-286

(Reiher 2001) Reiher, M.; Salomon, O.; Artur Hess, B. Theor. Chem. Acc. 2001, **107**, 48

(Schilt 1960) A. Schilt. Mixed Ligand Complexes of Iron(I1) and (111) with Cyanide and Aromatic Di-imines. J. Am. Chem. Soc. 1960, **82**, 3000-3005.

(Toma 1983) H. E. Toma, M. S. Takasugi. Spectroscopic Studies of Preferential and Asymmetric Solvation in Substituted Cyanoiron(ll) Complexes. *J. Sol. Chem.* 1983, **12,** 547-561.

(Tomasi 2005) J. Tomasi, B. Mennucci, and R. Cammi, "Quantum mechanical continuum solvation models," *Chem. Rev.*, 2005, **105**, 2999-3093. DOI: 10.1021/cr9904009

(Zhang 2016) W. Zhang, *et al.* Manipulating charge transfer excited state relaxation and spin crossover in iron coordination complexes with ligand substitution. *Chem. Sci.,* 2016, **8,** 515–523.